# High Metal Loading, Two Nanometer-Sized Platinum Zinc Intermetallic Nanoparticles from Atomically Dispersed Precursors for Hydrogenation Reaction

Siying Yu, † Ranjan Kumar Behera, ‡ Jung Hyun Park, † Shihyun Park, † Wenyu Huang, \*, ‡ Hong Yang\*, †

<sup>†</sup> Department of Chemical and Biomolecular Engineering, University of Illinois at Urbana-Champaign, 600 South Mathews Avenue, Urbana, IL 61801, USA

<sup>‡</sup> Department of Chemistry, Iowa State University, 2415 Osborn Drive, Ames, IA 50011, USA

\* Address correspondence to hy66@illinois.edu (HY), whuang@iastate.edu (WYH)

**Keywords:** ultrafine nanoparticle, intermetallic, platinum zinc, atomically dispersed precursor, hydrogenation reaction

#### **ABSTRACT**

Ultrafine intermetallic nanoparticles are attractive candidates as catalysts, especially in electrocatalysis and selective hydrogenation reactions. An intermetallic may possess stronger metal bonding and exhibit better chemical stability under harsh reaction conditions than its alloy counterpart, which exists as solid solution. Thermal treatment is often necessary for the preparation of intermetallic nanoparticles to achieve the required atomic ordering. Such processes are often carried out at elevated temperatures, which inevitably cause particle growth, resulting in broad distribution in structure and composition of nanoparticles (NPs). This change poses a challenge in obtaining uniformly deposited, ultrafine intermetallic NPs on supports. Here we report the control over particle size and uniformity of ultrafine PtZn intermetallic NPs using a dual-ligand metal-organic framework (MOF) as atomically dispersed precursors (ADPs) in a one-pot synthesis. Facecentered tetragonal (fct) 2.1 nm-sized L<sub>10</sub>-Pt<sub>50</sub>Zn<sub>50</sub> intermetallic NPs were produced after the thermal treatment. The simplicity of this synthesis allows us to study the effects of several key factors on particle size and uniformity. The resulting catalyst of L1<sub>0</sub>- Pt<sub>50</sub>Zn<sub>50</sub> on carbon has a Brunauer-Emmett-Teller (BET) surface area in the order of 150 m<sup>2</sup>/g. It acts as a highly selective hydrogenation catalyst for the liquid-phase conversion of 1-iodo-4-nitrobenzene and 1-bromo-4-nitrobenzene to the corresponding semi-hydrogenated products exclusively. Furthermore, the one-pot synthesis using ADPs allows for the preparation of ultrafine (<3 nm) bimetallic nanoparticles with a record high total metal mass loading of 29%, paving a way for the design of high metal loading intermetallic catalysts.

#### INTRODUCTION

Structurally ordered intermetallic nanoparticles (NPs) have attracted much interest as a new generation of catalysts with promising activity and durability, especially in several fast-growing fields, such as electrocatalysis<sup>1-5</sup> and selective hydrogenation.<sup>6, 7</sup> Incorporation of non-precious metals (M) into precious metals such as platinum (Pt) is desirable because of the considerations of not only sustainability and elemental abundance, but also improved activity and stability.8 It is common that Pt intermetallic NPs could achieve higher catalytic activity than pure Pt after the optimization of compositions and structures. In addition, on electrochemical durability, Pt-M intermetallic NPs are more stable<sup>10</sup> against oxidation or corrosion than their alloy counterparts, which are solid solutions of metal atoms. The enhanced stability stems in part from the atomically ordered structures and strong Pt-M bonding via d-electron interactions. 11 The stoichiometric nature with well-defined crystal unit cell and atomic ordering makes Pt-M intermetallic NPs an ideal catalyst to examine the structure-property relationship.<sup>12</sup> Recent studies reported enhanced catalytic activity and durability of ultrafine Pt-based NPs in both electrocatalysis<sup>13-16</sup> and selective hydrogenation.<sup>17, 18</sup> Therefore, the development of synthesis methodology for making ultrafine Pt-M intermetallic NPs could usher the development of highly active and durable catalysts on a unit mass basis and facilitate the understanding of reaction mechanism.

There are two general pathways to synthesizing Pt-M intermetallic NPs. One is to prepare alloy NPs in solution-phase, followed by heat treatment to convert them into intermetallic structures.<sup>1, 19</sup> The other method requires the use of wet impregnation approach to deposit metal precursors onto porous solid supports. Intermetallic NPs can be made after thermal treatment of the impregnated solid precursors.<sup>2, 3</sup> Since the formation of intermetallic NPs needs to overcome the energy barrier for atomic ordering,<sup>20</sup> high-temperature treatment (> 500 °C) is necessary in both cases, resulting in Ostwald ripening<sup>21</sup> and particle coalescence,<sup>22</sup> thus producing polydisperse NPs and making the preparation of ultrafine intermetallic NPs challenging. One strategy to overcome this technical hurdle is to disperse metal elements in three-dimensional space in order to facilitate the formation kinetics of intermetallics.<sup>20, 23</sup> Another approach is to incorporate a protective layer on the metal NP

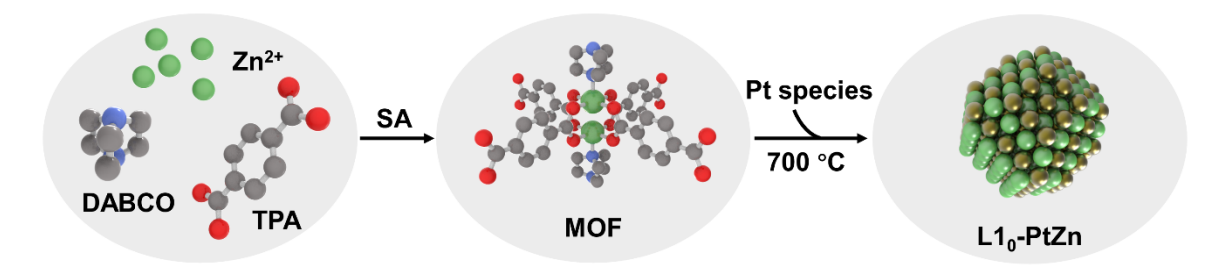
to prevent the particle overgrowth.<sup>2, 24</sup> However, there are few studies on making 2 nmsized intermetallic nanoparticles with tunable metal loading. Metal-organic frameworks (MOFs), a class of materials consisting of metal ions and organic ligands, <sup>25, 26</sup> may be an excellent structure to serve as the atomically dispersed precursors (ADPs), which accommodate metal species in the porous hierarchical structures. Besides the topotactic dispersion of reacting metal elements, MOFs could be simultaneously converted into carbon-based support for metal catalysts in situ during the pyrolysis step. Previously, MOFs such as zeolitic imidazolate framework (ZIF)-67 and ZIF-8 have been utilized in the preparation of supported metal nanoparticle<sup>27</sup> and single-atom catalysts.<sup>28,29</sup> Though many MOFs consist of a single organic ligand, a mix-ligand structure of two or more kinds of organic linkers introduces additional possibilities to tune the framework, porosity, and adsorbent properties.<sup>30</sup> For example, MOFs made from dicarboxylate and diamine ligands produce pillared-layer structures. In this dual-ligated MOF, dicarboxylates interact with metal ions to form the later structure, while the diamines function as the ligands for pillar. Thus, dual-ligand MOFs ensure the control of three-dimensional, porous hierarchical structures and are beneficial to the synthesis of ultrafine nanoparticles.

Herein, we report the synthesis of two nm-sized PtZn intermetallic NPs using dual-ligated MOFs as the ADPs via a one-pot synthesis. Compared with the size control of metal nanoparticles in solution-phase synthesis,<sup>31, 32</sup> the formation of metal NPs from MOF precursors is a solid state process, where Ostwald ripening and particle coalescence are more critical due to the slow diffusion rate of metal atoms in solid-phase precursors. In this sense, we explore the key factors in the controlled synthesis which lead to a high particle density and ultrafine size using ADP-based precursors. We produced face-centered tetragonal (*fct*) L1<sub>0</sub>-PtZn intermetallic NPs from 1,4-diazabicyclo[2.2.2]octane-terephthalic acid (DABCO-TPA) dual-ligand MOF after the thermal treatment. The resulting metal NPs supported on carbon exhibited two nm-sized pseudo-spherical shapes in a densely packed and uniform manner. We achieved a total metal loading up to 29 wt.% on carbon support for these MOF-derived ultrafine NPs under the optimized reaction conditions. The 2.1 nm-sized L1<sub>0</sub>-Pt<sub>50</sub>Zn<sub>50</sub>/C intermetallic NPs catalyst exhibits an exceptional selectivity and high conversion in the hydrogenation of 1-iodo-4-nitrobenzene and 1-bromo-4-nitrobenzene to 4-iodoaniline and 4-bromoaniline, respectively, showing

preferential hydrogenation of the nitro group (-NO<sub>2</sub>) group over the activation of the C-X (carbon-halogen) bond. We have also demonstrated that catalytic activity of L1<sub>0</sub>-PtZn/C catalysts in the hydrogenation of  $\alpha$ , $\beta$ -unsaturated aldehydes. PtZn intermetallic NPs were highly selective in hydrogenating C=O bonds over C=C bonds, resulting in unsaturated alcohols. On the contrary, commercial Pt/C exhibited a mixture of C=C and C=O hydrogenation products. This observation further highlights the necessity of the PtZn intermetallics phase in selective hydrogenation reactions.

#### RESULTS AND DISCUSSION

**Synthesis and Characterization of L1<sub>0</sub>-PtZn NPs.** The DABCO-TPA dual-ligand MOF with Zn<sup>2+</sup> as the cation center was used as the ADP in this study. **Scheme 1** illustrates the one-pot synthesis of L1<sub>0</sub>-phase intermetallic PtZn NPs from this kind of ADPs. In the preparation of DABCO-TPA dual-ligand MOF, Zn(NO<sub>3</sub>)<sub>2</sub>, DABCO, and TPA were first dispersed in dimethylformamide (DMF). Zinc ions coordinated with organic ligands, followed by a self-assembly (SA) to form Zn-DABCO-TPA MOFs (ZnDT) after the evaporation of DMF.<sup>30</sup> The as-prepared MOF served as the host structure for uniform deposition of Pt(acac)<sub>2</sub> in the framework via the wet impregnation. The Pt(acac)<sub>2</sub>-incorporated ZnDT (Pt/ZnDT) was then converted into intermetallic NPs at 700 °C with ramping rate of 2 °C/min through a vacuum pyrolysis process (**Scheme 1**). The use of vacuum significantly lowered the required processing temperature.



**Scheme 1.** Synthetic pathway of PtZn intermetallic NPs from ZnDT, which serves as the ADP.

Scanning electron microscopy (SEM) studies show the ZnDT has well-defined morphology (**Figure S1**). The X-ray diffraction (XRD) pattern of this MOF exhibits sharp peaks, suggesting large size of crystalline domain (**Figure S2**). Ultrafine and well-

dispersed NPs were produced from the Pt<sub>0.05</sub>/ZnDT at Pt(acac)<sub>2</sub>/ZnDT feeding ratio equal to 5/100 (atomic) using this procedure (**Figure 1a**). Carbon support formed simultaneously from the carbonization of the organic segments of the precursor. High-angle annular dark-field scanning transmission electron microscopy (HAADF-STEM) was applied to examine the intermetallic structure of as-made PtZn NPs (**Figure 1b**). The corresponding fast Fourier transform (FFT) image shows diffraction spots of facet (200) and facet (001) of *fct*-PtZn intermetallic with the *d*-spacing of 0.20 nm and 0.38 nm, respectively (inset of **Figure 1b**). Energy dispersive X-ray spectroscopy (EDS) was used to study the elemental distribution (**Figure 1c**). The Pt and Zn elemental maps overlapped with each other well, suggesting the excellent dispersion of both metal elements. The XRD pattern of the product fits well with that of the *fct*- PtZn (PDF#06-0604) (**Figure 1d**). The broadening of the XRD peaks implies relatively small domain size of these intermetallic NPs, which is consistent with the TEM study.

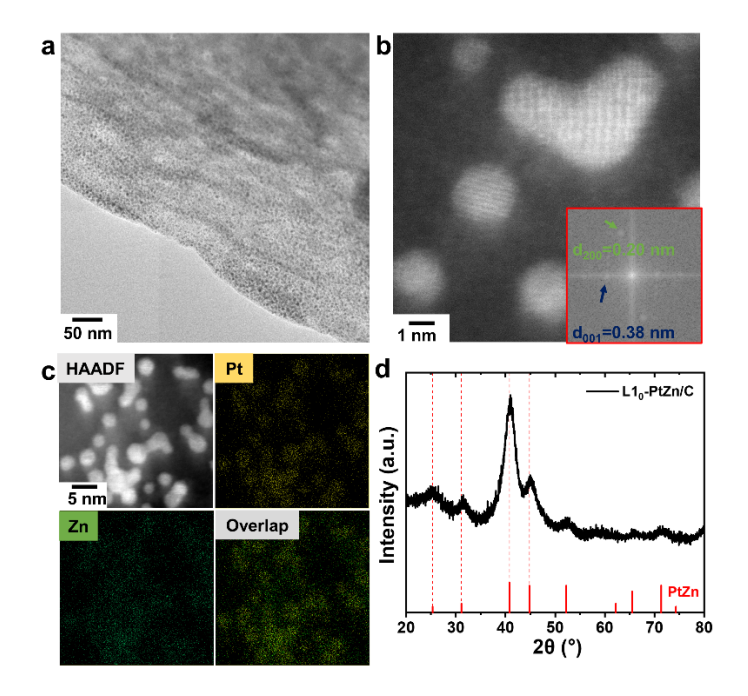


**Figure 1.** (a) Low-resolution TEM micrograph, (b) HAADF-STEM micrographs (inset: the corresponding FFT image), (c) STEM-EDS images, and (d) XRD pattern of as-made  $L1_0$ -Pt<sub>50</sub>Zn<sub>50</sub> NPs produced from Pt<sub>0.05</sub>/ZnDT through vacuum pyrolysis at 700 °C at a ramping rate of 2 °C/min.

Size and Composition of Ultrafine L1<sub>0</sub>-PtZn Intermetallic NPs. The as-prepared PtZn intermetallic NPs exhibited a very high packing density meanwhile having a uniform distribution in size and shape across the carbon support (Figure 2). Interestingly, the original morphology of the MOF remained after pyrolysis (Figure S3). We further noticed when the feeding ratios of Pt(acac)<sub>2</sub>/ZnDT were small (i.e., Pt<sub>0.01</sub>/ZnDT and Pt<sub>0.02</sub>/ZnDT), alloys were produced instead of intermetallic (Figure S4). To examine the ability of ZnDT in dispersing the Pt precursor and its effect on size and composition of the products, we carried out the synthesis at feed ratios of Pt(acac)<sub>2</sub>/Zn(NO<sub>3</sub>)·6H<sub>2</sub>O in the range of 5/100-20/100 (Pt/Zn atomic ratio) while keeping the amount of ZnDT the same. TEM study shows the formed NPs were uniform for all products made from  $Pt_x/ZnDT$  (x=0.05, 0.10, 0.15, and 0.20) (Figure 2a-2d). The average size of the NPs ranged from 2.0 nm for samples made from  $Pt_{0.20}/ZnDT$  to 2.6 nm from  $Pt_{0.05}/ZnDT$  (**Figure 2e-2h**). It appears the synthesis with the relatively large amount of Pt(acac)<sub>2</sub> in the feed resulted in the formation of small nanoparticles. The reason might be a short diffusion length of Pt atoms in the MOF at a high Pt loading amount. Average sizes of all samples were in the two nm-sized range. X-ray diffraction patterns of these PtZn NPs exhibited broad peaks, including the characteristic intermetallic diffractions centered at 25.4° and 31.1° (20) (Figure 2i).

SEM studies show the as-prepared PtZn intermetallic NPs on MOF-derived carbon supports retained their original morphologies (**Figure S5**). **Figure S6** shows the SEM image of the MOF product and the corresponding elemental maps of Pt and Zn. Both Pt and Zn signals distributed evenly across the entire MOF product. The metal compositions of products were further examined by both inductively coupled plasma optical-atomic emission spectroscopy (ICP-OES) (**Table S1**) and energy-dispersive X-ray fluorescence (XRF) (**Table S2**) techniques. The data obtained using these two methods agree with each other very well. For a relatively low Pt loading amount (*i.e.*, Pt<sub>0.05</sub>/ZnDT), the obtained NPs had a composition of Pt<sub>50</sub>Zn<sub>50</sub>, which agrees with the stoichiometry of the *fct* phase intermetallic. When the Pt(acac)<sub>2</sub>/ZnDT feeding ratio increased, the compositions became rich in Pt. The L1<sub>2</sub>-Pt<sub>3</sub>Zn intermetallic phase may locally exist beside the global ordered *fct* phase.

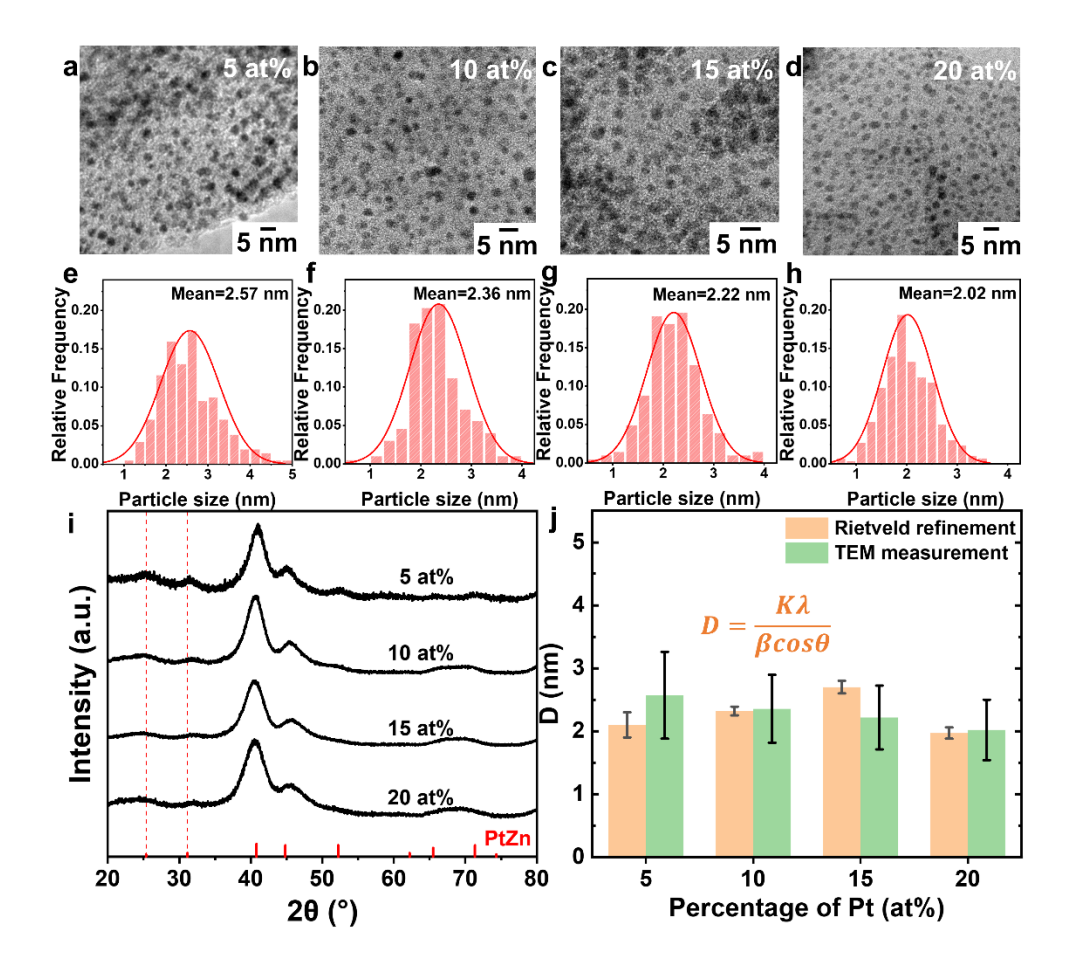


**Figure 2.** (a-d) TEM micrographs and (e-h) corresponding size distributions of PtZn NPs obtained from  $Pt_x/ZnDT$  at the x values of (a, e) 0.05, (b, f) 0.10, (c, g) 0.15, and (d, h) 0.20. (i) XRD patterns of the PtZn NPs obtained from the  $Pt_x/ZnDT$ . (j) Volume-weighted mean crystallite sizes (LVol-IB) calculated from Scherrer equation based on Rietveld refinement results, and measured crystal sizes along with corresponding errors for PtZn NPs with different Pt loading.

We used two methods to obtain mean sizes of these intermetallic Pt-Zn NPs. One is the direct measurement of diameter for over a hundred nanoparticles (**Table S3**) based on TEM data (**Figure 2e-2h**). The other is to calculate the volume-weighted mean crystallite size (LVol-IB) using Scherrer equation based on the XRD data (**Table S4**). To improve accuracy, we carried out Rietveld refinement to analyze the XRD patterns and obtain full-profile fittings using the TOPAS software. Similar values were obtained with these two methods and the average diameter of all particles were between 2.0 and 2.7 nm (**Figure 2j**). Compared with other reported PtZn NPs which were made through thermal treatments,

we produced uniform 2 nm-sized PtZn intermetallic NPs with metal loading up to 29 wt.% (**Table 1**). To the best of our knowledge, this value represents the highest metal loading among the known sub-3 nm PtZn intermetallic NPs produced. The ultrafine size (~2 nm) and uniform distribution that were enabled by using MOF-based precursors contributed to the observed high metal loading.

**Table 1.** Summary of reaction conditions, metal content and mean size of selected small L1<sub>0</sub>-PtZn intermetallic NPs.

Sample	T	Time	Metal content	Mean size*
	(°C)	(h)	(wt.%)	(nm)
PtZn/MWNT-E <sup>33</sup>	600	2	4.1	3.2
PtZn/NC <sup>34</sup>	800	3	25.3	5.1
$1Pt1Zn/MZ^{35}$	580	2	1.4	<3
PtZn/HNCNT <sup>6</sup>	800	1	0.82	2.24
Pt <sub>50</sub> Zn <sub>50</sub> (this work)	700	2	8.7	2.1
Pt <sub>63</sub> Zn <sub>37</sub> (this work)	700	2	29	2.0

<sup>\*</sup> Diameter

Study of the Reaction Conditions for Controlling the Ultrafine L1<sub>0</sub>-PtZn NPs. Besides the feeding ratio, we examined the effects of ramping rate ( $\dot{T}$ ) and pyrolysis temperature (T) on the particle size and uniformity. In a typical synthesis, the temperature of the furnace was raised to a pre-designated reaction temperature, *i.e.*, 700 °C at different ramping rates. Figure 3a shows the XRD patterns of the NPs produced from the precursors of Pt<sub>0.05</sub>/ZnDT mixtures at a ramping rate changing from 1 to 5 °C/min. Under these ramping rates, PtZn intermetallic NPs formed, judging by the characteristic XRD peaks centered around 25.4° and 31.1° 20. The atomic ratio between Pt and Zn is either 50:50 or close to this value (Table S5). The Pt<sub>50</sub>Zn<sub>50</sub> matched the stoichiometry of tetragonal L1<sub>0</sub> phase PtZn intermetallic. There is no strong correlation between the stoichiometry of PtZn and the ramping rate of heat treatment. For the sample produced at 5 °C/min, however, the XRD peaks shifted slightly, and the apparent composition also changed to Pt<sub>69</sub>Zn<sub>31</sub>. Such a large deviation from 50:50 suggests a severe loss of Zn at a high ramping rate. The removal of Zn element during the heat treatment may be attributed to the vaporization of Zn atoms and

the decomposition of zinc oxide (ZnO). The application of vacuum reduced the pressure of the reaction chamber to ~10<sup>-5</sup> atm, thus facilitated the vaporization of Zn.<sup>36</sup> The trace amount of water in the tube furnace might catalyze the decomposition of ZnO, further lowering the reaction temperature required for Zn removal,<sup>37</sup> which was below the typical pyrolysis temperature when Zn was used as a sacrificial metal.<sup>29</sup> The small amount of water molecules should come from the decomposition of ADPs and could remain in the furnace, if not promptly removed. The slow removal of water may contribute to the severe loss of Zn at 5 °C/min. Thus, other than the formation of *fct* L1<sub>0</sub> intermetallic structure, the product might contain Pt-enriched face-centered cubic (*fcc*) phase L1<sub>2</sub>-Pt<sub>3</sub>Zn (or Pt<sub>75</sub>Zn<sub>25</sub>) intermetallic, judging by the XRD pattern.

Our data further indicates a moderate ramping rate produced ultrafine and uniform PtZn intermetallic NPs. We found there was a good agreement in the analysis of particle size between the TEM and XRD studies (**Figure 2j**), thus we used the latter method directly to obtain the mean size of NPs (**Table S6**). The size of the NPs reached the minimum at the ramping rate of 2 °C/min (**Figure 3b**). At the slowest ramping rate of 1 °C/min, we observed ultrafine primary nanoparticles in the TEM micrograph (**Figure S7a**), though NPs might also sinter (**Figure 3c**). It appears when a low ramping rate was used in the synthesis, the reaction time increased substantially, facilitating the migration of small NPs on the formed carbon support to sinter, giving rise to the formation of large aggregates. When the ramping rate was 5 °C/min, the formed NPs exhibited sharp peaks in the XRD pattern, suggesting the NPs became polydisperse (**Figure 3d, S7b-c**). Both small and large NPs formed in the same sample, indicating local reaction rates differed throughout the solid.

The high pyrolysis temperature (700 °C) inevitably caused the Ostwald ripening in the solid-state preparations. We used the Gibbs-Thomson equation to analyze the effect of the key processing parameter, namely, the pyrolysis temperature T on the final structures of NPs. In this treatment, the equilibrium concentration of solute atoms  $C_{eq}(r)$  depends on the size of nanoparticles:

$$C_{eq}(r) = C_{eq}(\infty) \exp\left(\frac{2\sigma v_{at}}{rk_B T}\right) \tag{1}$$

where  $C_{eq}(\infty)$  is the solubility of atoms taken from an infinite flat surface,  $\sigma$  is surface tension,  $v_{at}$  is atomic volume, r is the radius of the nanoparticle,  $k_B$  is Boltzmann constant and T is temperature. The chemical potential  $\mu$ , which is closely related to the equilibrated concentration, can be written as:

$$\mu = k_B T \ln \left[ C_{eq}(r) \right] = \frac{2\sigma v_{at}}{r} \ln \left[ C_{eq}(\infty) \right]$$
 (2)

The temperature gradient across the impregnated MOF precursors may result in different local reaction rates. Such differences in the formation process produced NPs with varied sizes. Thus, the discrepancy in chemical potential between two NPs  $(r_1 \text{ and } r_2)$  should be:

$$\Delta \mu = \mu_1 - \mu_2 = 2\sigma v_{at} \ln \left[ C_{eq}(\infty) \right] \left( \frac{1}{r_1} - \frac{1}{r_2} \right)$$
 (3)

Primary metal NPs produced in the region with slow reaction rates have small size ( $\sim$ 2 nm) as observed in **Figure S7a**, while those produced in the fast reaction region should have large size (**Figure S7b**). This variance in particle sizes results in a difference in chemical potential. Since temperature gradient is caused by ramping rate  $\dot{T}$ , and the right side of equation (3) is related to the mean size D, we can correlate ramping rate with particle size and uniformity in the following equation:

$$\Delta\mu(\dot{T}) = 2\sigma v_{at} \ln\left[C_{eq}(\infty)\right] \left(\frac{1}{r_1} - \frac{1}{r_2}\right) = constant \times g(D)$$
(4)

This analysis suggests under relatively fast ramping rates, Ostwald ripening could dominate, resulting in the large mean size and broad size distribution.

Our data shows the size of PtZn intermetallic NPs was uniform at the low ramping rate of  $1 \, ^{\circ}$ C/min using the ADP-based synthesis. Ostwald ripening became increasingly important when the ramping rate increased, resulting in temperature gradient across the Pt<sub>0.05</sub>/ZnDT precursor mixtures. Under such processing conditions, both particle mean size and size distribution increased (**Figure 3b**). The observed relationship between mean size *D* and ramping rate  $\dot{T}$  agrees well with the exponential relationship between reaction rate and temperature, based on the above analyses:

$$\frac{\partial D}{\partial \dot{\tau}} > 0, \frac{\partial^2 D}{\partial \dot{\tau}^2} > 0 \tag{5}$$

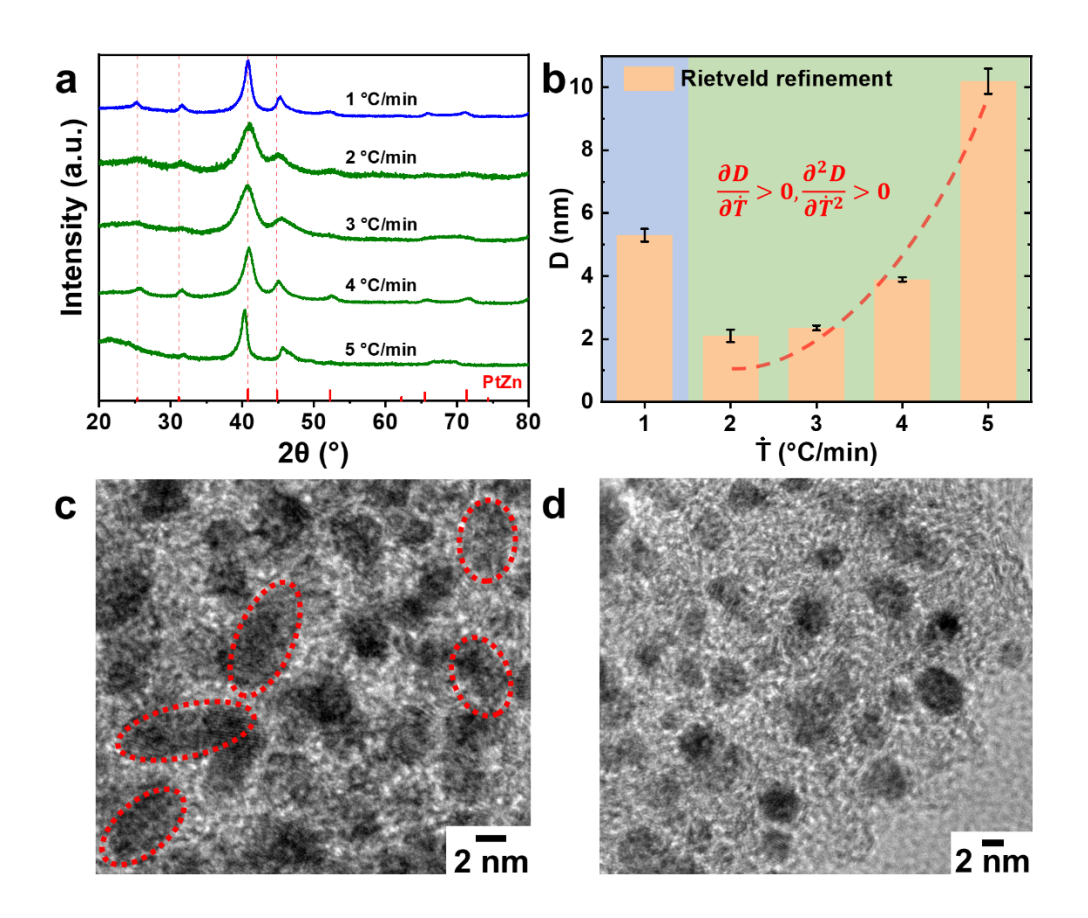


**Figure 3.** (a) XRD patterns, (b) relationship between size and ramping rate, and (c, d) TEM micrographs of PtZn intermetallic NPs made through vacuum pyrolysis at 700 °C. The TEM specimen were made using NPs formed at a ramping rate of (c) 1 and (d) 5 °C/min, respectively.

Another crucial factor in the formation of PtZn intermetallic structures is reaction temperature. We performed a series of experiments at different reaction temperatures to find out the upper and lower limit of producing intermetallic NPs. Platinum zinc intermetallic began to form at 600 °C (**Figure 4a**), and only a mixture of ZnO and Pt nanoparticles was observed when the reaction temperature was 500 °C (**Figure S8**). The XRD peaks matched very well with the tetragonal phase of PtZn intermetallic for sample made at a temperature between 600 °C and 700 °C. For the NPs formed at 750 °C, the (111) diffraction peaks at ~41° 20 for PtZn intermetallic shifted, as is indicated by the dash line in **Figure 4a**. This shift indicates the phase transformation towards the *fcc* phase of the

Pt<sub>3</sub>Zn intermetallic structure. When the reaction temperature was raised to 800 °C, *fcc* Pt NPs formed due to the severe loss of Zn (**Table S7**).

While reaction temperature affected greatly the sizes, its effect on the particle uniformity was much less pronounced, based on the calculation of domain size from XRD patterns (**Table S8**). When the temperature changed from 600 °C to 750 °C, the particle size monotonically increased (**Figure 4b**). The size dropped while the uniformity remained when temperature further increased from 750 °C to 800 °C. The drop in size should be the result of loss of Zn at higher temperature. TEM study shows the NPs are still uniformly distributed on the supports in the temperature range between 600 °C and 750 °C (**Figure 4c** and **4d**).

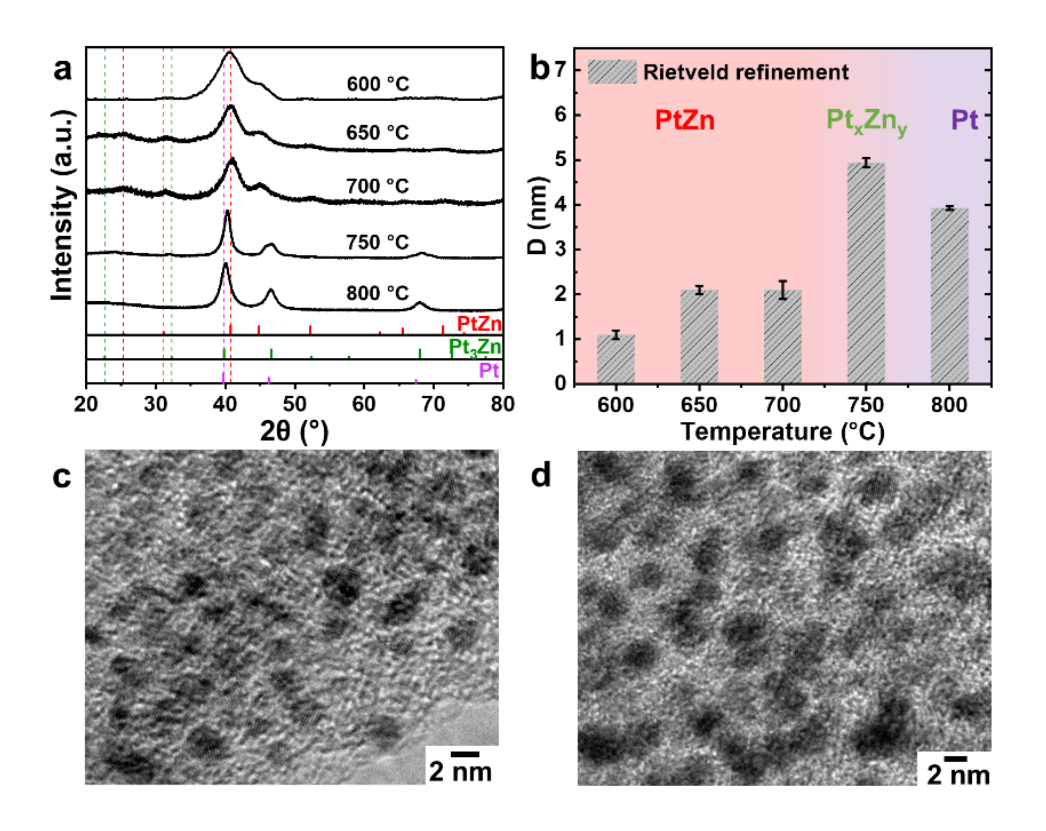


**Figure 4.** (a) XRD patterns and (b) calculated sizes of the Pt-Zn NPs made from Pt<sub>0.05</sub>/ZnDT at different reaction temperatures (ramping rate: 2°C/min). TEM micrographs of PtZn intermetallic NPs produced at (c) 600 °C, and (d) 750 °C, respectively.

Size control of intermetallic NPs is related to the reduction of the metal salts and the formation of ordered alloy phase between the two, thus the rate of reduction reaction is

important. In this context, we examined the products from the heat treatment of Pt<sub>0.05</sub>/ZnDT at 700 °C (ramping rate: 2 °C/min) under both pure Ar and 5%H<sub>2</sub> in Ar forming gas atmospheres. The obtained NPs on carbon are denoted as PtZn-A (pure Ar atmosphere) and PtZn-H (5% H<sub>2</sub> in Ar atmosphere), respectively. The XRD patterns of the resulting products show the formation of fct PtZn intermetallic (**Figure S9**). If the thermal treatment was performed under pure Ar, organic linkers decomposed and acted as reducing agent at the same time to convert the metal ions into intermetallic NPs. In the absence of reducing gas and vacuum, a good amount of Zn cation might be oxidized to form ZnO particles, as is shown by the sharpened XRD peaks. TEM study shows the NPs of PtZn-A exhibited a bimodal distribution in size. The FFT analysis shows the large NP (purple box) had a dspacing of 0.25 mm, which fits well with (101) facet of ZnO, and the ultrafine NP (red box) had a d-spacing of 0.22 nm, which can be attributed to the (111) diffraction of fct PtZn intermetallic (Figure S10). Large ZnO and ultrafine PtZn intermetallic NPs formed simultaneously, suggesting the mild reducing agent should be a key factor for the formation of ultrafine NPs. Interestingly, the carbon support produced in this one-pot synthesis retained the MOF morphology (Figure S11).

When forming gas was used in the synthesis, hydrogen gas effectively reduced Zn cations to form *fct* PtZn intermetallic NPs (**Figure S9**). TEM micrograph shows large NPs formed at this temperature, when hydrogen gas was used as reducing agent (**Figure S12**). These results suggest fast reaction rate causes decomposition of MOF precursors and the collapse of carbon structure.

**Figure 5** summarizes the key factors for the production of ultrafine PtZn intermetallic NPs using ZnDT as ADP. There exists a strong interplay among the pyrolysis temperature, reducing atmosphere, ramping rate and reaction time. A moderate ramping rate is significant in preparation of ultrafine and uniform PtZn intermetallic NPs. Fast heating causes temperature gradient, giving rise to the Ostwald ripening. Slow heating may trigger sintering of primary NPs. Both ripening and sintering may result in large size, broad size distribution and polydispersity. When mild reducing agents are used, reaction temperature becomes important in determining the crystal structure of final products with different Pt/Zn ratios.

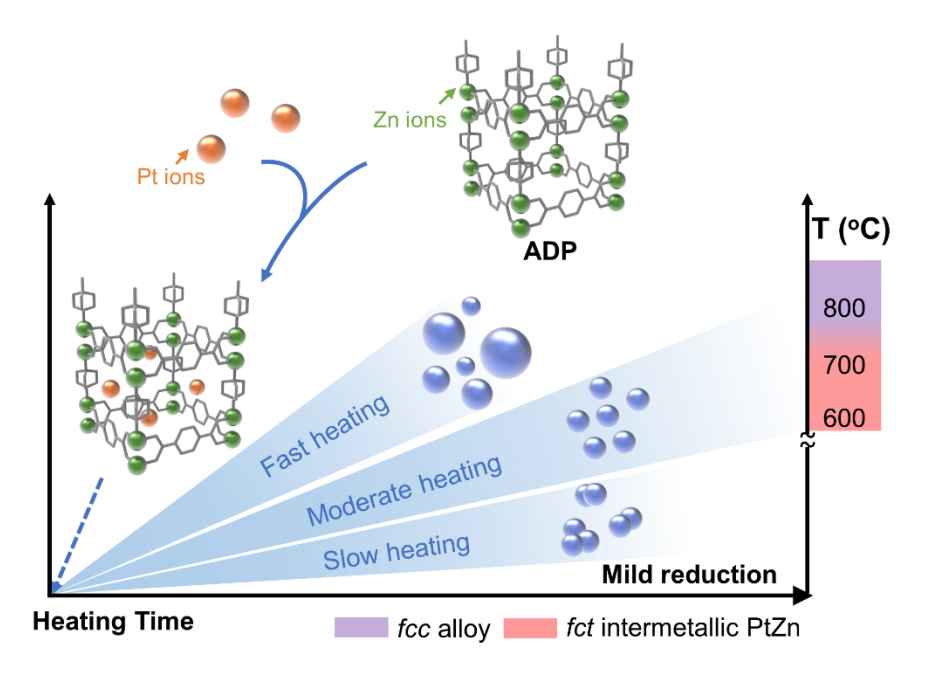
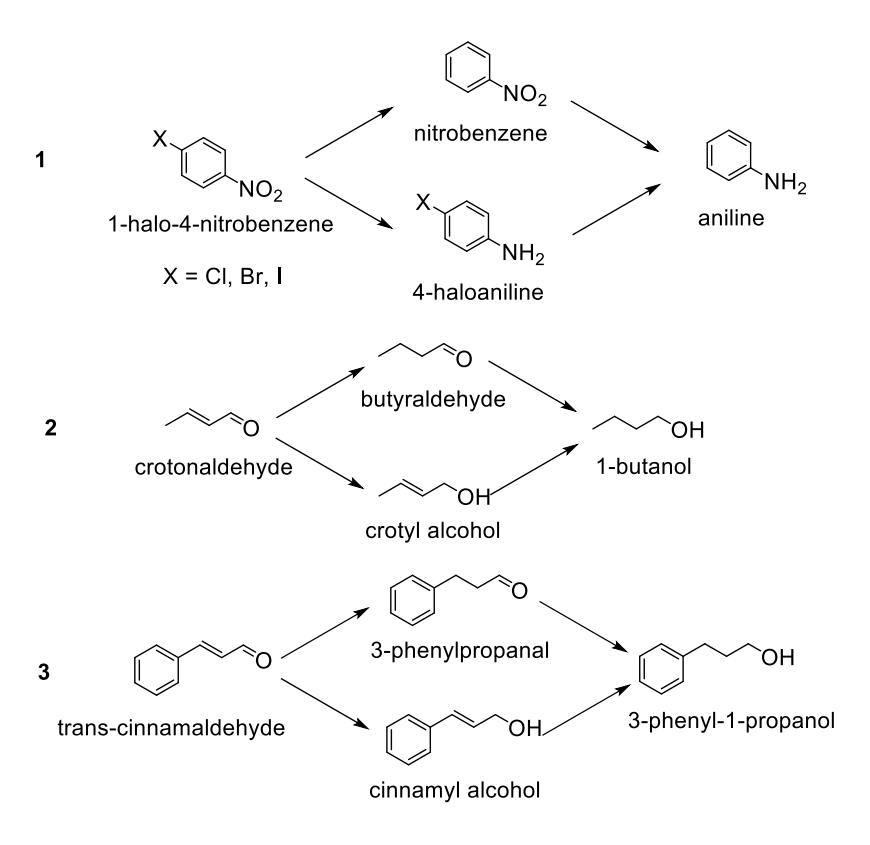


**Figure 5.** Illustration of the formation of ultrafine PtZn intermetallic NPs from the Pt/ZnDT and the effects of key reaction parameters on size and uniformity.

The catalytic selectivity of the L1<sub>0</sub>-Pt<sub>50</sub>Zn<sub>50</sub> catalyst were evaluated in the liquid phase hydrogenation reactions of 1-halo-4-nitrobenzene, crotonaldehyde, and transcinnamaldehyde (**Scheme 2**). **Figure S13** shows the results of nitrogen isotherm analysis of the carbon-supported 2.1 nm-sized L1<sub>0</sub>-Pt<sub>50</sub>Zn<sub>50</sub> intermetallic catalyst made from Pt<sub>0.05</sub>/ZnDT in 700 °C under vacuum pyrolysis (ramping rate: 2 °C/min). The isotherm results show that this catalyst has a mesoporous structure with BET surface area of 156 m<sup>2</sup>/g and an average pore diameter of 3.6 nm (BJH), suggesting it as a promising heterogeneous catalyst in the hydrogenation reaction.



**Scheme 2.** Liquid phase hydrogenation of (1) 1-halo-4-nitrobenzene, (2) crotonaldehyde, and (3) trans-cinnamaldehyde catalyzed by the ultrafine  $L1_0$ -Pt<sub>50</sub>Zn<sub>50</sub> catalyst.

We reported our findings from the liquid phase hydrogenation of 1-halo-nitrobenzenes on 2.1 nm-sized L1<sub>0</sub>-Pt<sub>50</sub>Zn<sub>50</sub> catalyst in **Figure 6.** The experiments were intended to study the hydrogenation selectivity between C-X and -NO<sub>2</sub> groups. The ultrafine ultrafine L1<sub>0</sub>-Pt<sub>50</sub>Zn<sub>50</sub> catalyst exhibited exceptionally high conversion of >99% and high selectivity to 4-haloaniline (98-99%) (**Figure 6a**). In contrast, a commercial 5% Pt/C catalyst, though exhibited >99% conversion for 1-halo-4-nitrobenze, had a much lower selectivity to desired product, 4-iodoaniline (20.8%), 4-bromoaniline (33.5%), and 4-chloroaniline (52.3%), respectively. It has been previously demonstrated that PtZn intermetallics are chemoselective for the liquid phase hydrogenation of 1-halo-4-nitrobenzene to corresponding haloanilines.<sup>38</sup> The addition of Ga and Zn enhances the performance of Pt-based bimetallic catalysts by donating electrons to Pt, *i.e.*, the proposed active sites. In our case, the exceptional high chemoselectivity to haloaniline in the case of ultrafine L1<sub>0</sub>-Pt<sub>50</sub>Zn<sub>50</sub> catalyst would also origin from the electron-enriched Pt in PtZn catalysts, increasing the selectivity of haloaniline above 99%.<sup>38</sup> The slightly lowered selectivity for

1-iodo-4-nitrobenzene could be the result of strong adsorption of iodine on Pt surface,<sup>39, 40</sup> which leads to dehalogenated aniline side-product. **Table S9** summarizes the results of the performances of this catalyst, together with a reference Pt catalyst.

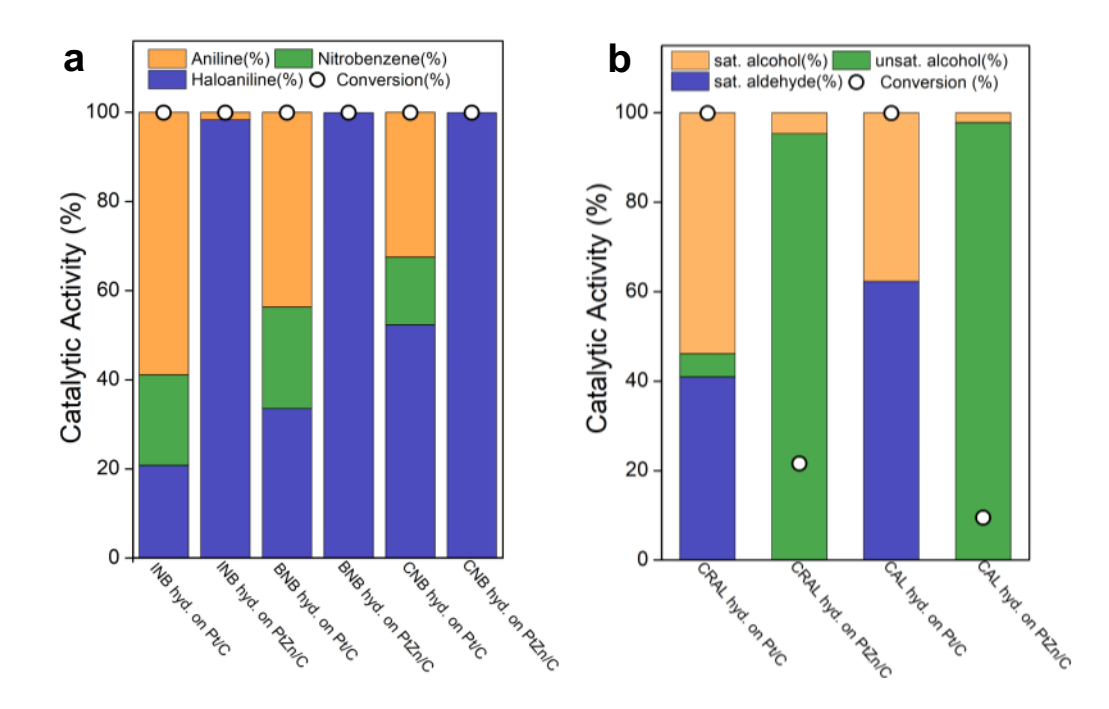


**Figure 6.** Conversion and selectivity of liquid phase hydrogenation reactions: (a) hydrogenation of 1-iodo-4-nitrobenzene (INB), 1-bromo-4-nitrobenzene (BNB), and 1-chloro-4-nitrobenzene (CNB); (b) hydrogenation of crotonaldehyde (CRAL) and transcinnamaldehyde (CAL) on 2.1 nm-sized L1<sub>0</sub>-Pt<sub>50</sub>Zn<sub>50</sub> intermetallic NPs and 5% Pt catalysts. Reaction conditions for (a): 0.4 mmol of 1-halo-4-bromobenzene, 2 mL toluene, 20 mg xylene as internal standard, 80 °C, 20 bar H<sub>2</sub>, 600 rpm, 12 h. Reaction conditions for (b): 1.2 mmol of  $\alpha$ ,β-unsaturated aldehydes, 1.2 mL toluene, 20 μL mesitylene as internal standard, 100 °C, 20 bar H<sub>2</sub>, 600 rpm, 12 h.

Another typical kind of chemoselective hydrogenation reaction is from  $\alpha$ ,  $\beta$ -unsaturated aldehydes/ketones to unsaturated alcohols, as shown in **Figure 6b** and **Table S10**. Previously reported Pt-based bimetallic catalysts have shown to be promising candidates for the hydrogenation reaction of  $\alpha$ ,  $\beta$ -unsaturated aldehydes, though high selectivity is still lacking. The selectivity of monometallic Pt and the ultrafine L1<sub>0</sub>-Pt<sub>50</sub>Zn<sub>50</sub> catalysts are compared in the hydrogenation of crotonaldehyde and trans-cinnamaldehyde (**Scheme 2**). Commercial Pt exhibited higher conversion in both crotonaldehyde and trans-

cinnamaldehyde hydrogenation, however, the L1<sub>0</sub>-Pt<sub>50</sub>Zn<sub>50</sub> catalyst outperformed Pt catalysts in the outstanding selectivity towards crotyl alcohol (95.3%) and cinnamyl alcohol (97.8%). The inferior selectivity of Pt catalysts are caused by the formation of C=C products (butyraldehyde and 3-phenylpropanal) hydrogenation and complete hydrogenation products (1-butanol and 3-phenyl-1-propanol). This enhanced hydrogenation selectivity for C=O bonds over C=C bonds can be attributed to the different adsorption configurations of  $\alpha$ ,  $\beta$ -unsaturated aldehydes on intermetallic surfaces. <sup>45-47</sup> For example, on the Pt(111) surface, both C=C and C=O bonds can be adsorbed via the two σorbitals (di- $\sigma$  mode) or the  $\pi$ -orbital ( $\pi$ -mode), while C=O can solely attaches to the Pt sites by an "end-on" mode, where only the oxygen end is captured by the surface Pt site. Such "end-on" mode facilitates the preferential hydrogenation of C=O bond and yields the desired hydrogenation products. Meanwhile, the pure Pt catalysts and our ultrafine L1<sub>0</sub>-Pt<sub>50</sub>Zn<sub>50</sub> intermetallic catalysts differ in the surface atomic ordering. The contiguous Pt ensembles of the pure Pt catalysts are advantageous for the hydrogenation of di-σ-mode adsorption while the  $\pi$ -mode and the "end-on" mode only requires single atomic site thus is preferable in the intermetallic system. Based on the discussion above, we propose the intermetallic surface can give rise to reactant taking preferential perpendicular adsorption of C=O on the active site, leading to unsaturated alcohol products.<sup>48</sup> Interestingly, the selectivity of trans-cinnamaldehyde to cinnamyl alcohol (97.8%, **Table S10**) is higher than that of crotonaldehyde to crotyl alcohol (96.35%, Table S10). The slightly higher selectivity to unsaturated alcohol suggests the hinderance effect of the phenyl, which may contribute to the preferable "end-on" mode adsorption.

#### **CONCLUSION**

We developed a facile one-pot synthesis for making two nm-sized PtZn intermetallic NPs from ZnDT, which was used as ADP. Using ADP approach, the ultrafine PtZn intermetallic NPs (< 3nm) could have a high metal loading up to 29 wt.%. Ramping rate, reaction temperature, and reducing agents can all affect the particle size and uniformity. Moderate ramping rate, uniform heating, and optimized reaction time could effectively prevent Ostwald ripening and particle sintering. Using MOF-based precursors could result in the simultaneous formation of mesoporous carbon supports. The 2.1 nm-sized L1<sub>0</sub>-Pt<sub>50</sub>Zn<sub>50</sub>

intermetallic NPs catalyst showed excellent selectivity in the liquid phase hydrogenation of several types of unsaturated hydrocarbon derivatives, with preferable activity in the carbonyl and nitro group over the carbon double bond. This study highlights the advantage of using ADP in the preparation of ultrafine bimetallic nanostructures, paving a way for the design of catalysts where both atomic ordering and high metal loading are important.

#### **EXPERIMENTAL SECTION**

Chemicals and Materials. Zinc nitrate hexahydrate  $(Zn(NO_3)_2 \cdot 6H_2O)$  (98%, reagent grade), terephthalic acid (TPA) (98%), 1,4-diazabicycyclo[2,2,2]octane (DABCO) (ReagentPlus,  $\geq$  99%), 1-iodo-4-nitrobenzene (98%), 1-chloro-4-nitrobenzene(99%), toluene (anhydrous, 99.8%), and p-xylene (anhydrous, 99+%) were purchased from Sigma Aldrich. Trans-cinnamaldehyde (99%), crotonaldehyde (99%), and mesitylene (99%) were purchased from Acros Organics. 1-bromo-4-nitrobenzene (98%) was purchased from Alfa Aesar. Dimethylformamide (DMF) (D131-4) was obtained from Fisher Chemical. Platinum (II) acetylacetonate (Pt(acac)<sub>2</sub>) (98%) was purchased from Strem Chemicals. Argon (UHP), and 5% hydrogen balance argon (certified standard mixture) were supplied by Airgas, Inc. All chemicals and gases were used without further purification.

Synthesis of ZnDT. In a typical synthesis of MOF precursor, Zn(NO<sub>3</sub>)<sub>2</sub>·6H<sub>2</sub>O (480 mg, 1.61 mmol), DABCO (548.2 mg, 4.89 mmol), and 15 mL DMF were mixed in a three-neck 50 mL flask. The flask was placed in an aluminum heating block on the hotplate/stirrer (VWR 7x7 Ceramic Hotplate Stirrer 97042-714) which was preheated to 150 °C. In a separate 50-mL beaker, TPA (803.4 mg, 4.86 mmol) was dissolved in 10 mL DMF before adding to the flask, followed by another addition of 10 mL DMF. The total volume of DMF in the flask was 35 mL. Two openings of the flask were sealed with glass stoppers, and the central opening was connected to a condenser with running cold water. After the mixture was stirred at 400 rpm and heated at 150 °C for two hours, the condenser was removed to evaporate all the solvent. The dried product was collected in a 50-mL centrifuge tube and washed by 35 mL of warm DMF (~150 °C). The solid product was separated from the liquid by centrifugation at 9000 rpm for 10 min (Beckman Coulter Inc., Allegra X-30

Series). The washing and centrifugation step was repeated at least three times until the supernatant was colorless and transparent. The wet solids were then dried at 80 °C in a vacuum oven (VWR Symphony, Cat. No. 414004-582) overnight to obtain the ZnDT.

**Synthesis of L1<sub>0</sub>-Pt<sub>50</sub>Zn<sub>50</sub> Intermetallic Nanoparticles on Carbon by Vacuum Pyrolysis.** In a typical synthesis, Pt(acac)<sub>2</sub> (31.2 mg, 0.08 mmol) at 5/100 atomic ratio of Pt/ZnDT was dissolved in 1 mL of DMF by sonication and added to 950 mg of as-prepared ZnDT in a mortar. A glass stick was used to stir the mixture with MOF until a slurry was formed without visible particles. This slurry was dried at 80 °C in a vacuum oven for 30 min. till dry. The dried solid was ground into fine powder and transferred into an alumina combustion boat. The boat was placed inside an air-tight tube furnace (MTI Corporation, GSL-1500X) and purged with Ar for 30 min. After the purge, the vacuum was pulled for 30 min using a vacuum pump (Edwards RV12) before the temperature of the furnace was raised from room temperature to 700 °C at a ramping rate of 2 °C/min. The alumina boat was kept at 700 °C in vacuum for 2 h, followed by cooling naturally to room temperature. The final product was collected for further use and characterization.

**Synthesis of PtZn Intermetallic Nanoparticles on Carbon under Different Reaction Conditions.** Preparations with predetermined amounts of  $Pt(acac)_2$  other than  $Pt(acac)_2/ZnDT$  precursor atomic ratio of 5/100 were carried out to study the key processing parameters on the formation of ultrafine PtZn intermetallic nanoparticles. The amounts of  $Pt(acac)_2$  used were 6.3 mg ( $Pt_{0.01}/ZnDT$ ), 12.7 mg ( $Pt_{0.02}/ZnDT$ ), 63.3 mg ( $Pt_{0.10}/ZnDT$ ), 95.0 mg ( $Pt_{0.15}/ZnDT$ ), and 126.6 mg ( $Pt_{0.20}/ZnDT$ ), respectively. The wet impregnation steps for  $Pt_x/ZnDT$  (x=0.01, 0.02, 0.05) were the same, while those for  $Pt_x/ZnDT$  (x=0.10, 0.15, 0.20), both the impregnation and drying steps were repeated for two, three, and four times, respectively. Each time 31.2 mg of  $Pt(acac)_2$  was dissolved in 1 mL of DMF and added to the MOF to form a slurry.

Besides the Pt(acac)<sub>2</sub>/ZnDT atomic ratio, we studied the effect of ramping rate at 1, 3, 4, and 5 °C/min, respectively, to reach the reaction temperature of 700 °C. In addition, we tested the formation at a temperature of 500, 600, 650, 750, and 800 °C, respectively. The ramping rate was kept as 2 °C/min for the different reaction temperatures.

In addition to vacuum pyrolysis, both pure argon and forming gas of 5%H<sub>2</sub> in Ar were also tested for the synthesis. The corresponding final products were denoted as PtZn/C-A for samples treated in pure Ar and PtZn/C-H for samples treated in forming gas of 5%H<sub>2</sub> in Ar.

Structural and Compositional Characterization. Powder X-ray diffraction (XRD) patterns were obtained using Rigaku Miniflex 600 diffractometer with Cu Kα X-ray source (λ =1.54056 Å). Scanning electron microscopy (SEM) images and energy dispersive spectrometry (EDS) elemental mapping were taken using Hitachi S-4800 high resolution microscope and Oxford's Ultim Max 100 mm² large area silicon drift detector. Transmission electron microscopy (TEM) micrographs were obtained on JEOL 2100 Cryo microscope at an accelerating voltage of 200 kV. The atomic ratio of Pt/Zn in the samples were determined by Shimadzu EDX-7000 energy-dispersive X-ray fluorescence (XRF) spectrometer and from inductively coupled plasma optical-atomic emission spectroscopy (ICP-OES) using a PerkinElmer Optima 8300 system.

**Size Analysis Based on X-Ray Diffraction.** Rietveld refinement of XRD patterns and the corresponding size analyses were carried out using TOPAS, a profile fitting software provided by Bruker Corporation. Scherrer equation was used to calculate the volume-weighted mean crystallite size (LVol-IB) using full-profile peaks, calculated by the built-in size estimation functions (**Figure S14-25**).

#### Catalytic Performance Tests of Liquid Phase Hydrogenation.

Hydrogenation reactions were performed in a high-pressure reactor. Before each reaction, the L1<sub>0</sub>-Pt<sub>50</sub>Zn<sub>50</sub>/C catalyst was pre-treated at 300 °C for 1 h under 10% H<sub>2</sub>/Ar. In a typical hydrogenation reaction of crotonaldehyde or trans-cinnamaldehyde, 5 mg of L1<sub>0</sub>-Pt<sub>50</sub>Zn<sub>50</sub>/C catalyst was added to a one-dram vial containing a solution of 1.2 mmol of substrate (crotonaldehyde or trans-cinnamaldehyde), 20  $\mu$ L of mesitylene as internal standard and 1.2 mL of toluene as solvent. The reaction mixture was loaded inside a stainless-steel autoclave, and 20 bar H<sub>2</sub> was used to purge the reactor five times. The hydrogenation reaction was carried out at 100 °C, under 20 bar H<sub>2</sub>, and stirred at 600 rpm for 12 h.

For the hydrogenation of nitrobenzene compounds, 5 mg of L1<sub>0</sub>-Pt<sub>50</sub>Zn<sub>50</sub>/C catalyst was added to a one-dram vial containing a solution of 0.4 mmol of halonitrobenzene substrate (1-iodo-4-nitrobenzene, 1-bromo-4-nitrobenzene, or 1-choloro-4-nitrobenzene), 22.8  $\mu$ L of xylene as internal standard and 2.0 mL of toluene as solvent. The reaction mixture was loaded inside a stainless-steel autoclave, and 20 bar H<sub>2</sub> was used to purge the reactor five times. The hydrogenation reaction was carried out at 80 °C, under 20 bar H<sub>2</sub>, and stirred at 600 rpm for 12 h.

The product mixture was analyzed in a HP 6890 series gas chromatogram (GC) equipped with a capillary column HP-5 and a flame ionization detector (FID) and a HP 6890N GC-mass spectrometer (MS) equipped with a capillary column HP-5MS.

## ASSOCIATED CONTENT

# **Supporting Information**

Supporting Information is available free of charge.

SEM image and XRD pattern of ZnDT. XRD patterns, SEM images and TEM micrographs, ICP-OES data, XRF data, and tables on size analysis of as-made Pt-Zn NPs. Tables on liquid phase hydrogenation reaction (reaction conditions, and performance data) of the Pt<sub>50</sub>Zn<sub>50</sub> intermetallic catalyst.

#### **AUTHOR INFORMATION**

## **Corresponding Authors**

Hong Yang – Department of Chemical and Biomolecular Engineering, University of Illinois at Urbana-Champaign, Urbana, Illinois 61801, United States; ID: orcid.org/0000-0003-3459-4516; Email: hy66@illinois.edu

Wenyu Huang – Department of Chemistry, Iowa State University, Ames, IA 50011-1021, United States; ID: orcid.org/0000-0003-2327-7259; Email: whuang@iastate.edu

#### Authors

Siying Yu – Department of Chemical and Biomolecular Engineering, University of Illinois at Urbana-Champaign, Urbana, Illinois 61801, United States

Ranjan Kumar Behera – Department of Chemistry, Iowa State University, Ames, IA 50011-1021, United States

Jung Hyun Park – Department of Chemical and Biomolecular Engineering, University of Illinois at Urbana-Champaign, Urbana, Illinois 61801, United States

Shihyun Park – Department of Chemical and Biomolecular Engineering, University of Illinois at Urbana-Champaign, Urbana, Illinois 61801, United States

#### **Author contributions**

**S. Y.** conceptualization, methodology, writing – original draft, writing – review & editing, data curation, validation, analysis. **R. K. B.** data curation, writing – review & editing. **J. H. P.** writing – review & editing. **S. P.** data curation. **W. H.** investigation, resources, writing – review & editing. **H. Y.** supervision, conceptualization, investigation, resources, funding acquisition, writing – review & editing.

#### Notes

The authors declare no competing financial interest.

#### ACKNOWLEDGMENTS

This work was funded in part by the Alkire Chair Professorship from the University of Illinois. W.H. acknowledges the support from National Science Foundation (CHE-2108307) and Iowa State University Trapp Award. Electron microscopy characterization and X-ray fluorescence characterization were carried out in the Materials Research Laboratory Central Research Facilities, University of Illinois. Powder X-ray diffraction was performed in the George L. Clark X-ray Facility and 3M Materials Laboratory in School of Chemical Sciences (SCS) at the University of Illinois, Urbana Champaign (UIUC). Inductively coupled plasma optical-atomic emission spectroscopy was carried

out in the Microanalysis Laboratory in SCS, UIUC. We would like to thank Dr. Danielle Gray and Dr. Toby Woods for their help with XRD analysis.

#### REFERENCES

- (1) Li, J.; Sharma, S.; Liu, X.; Pan, Y.-T.; Spendelow, J. S.; Chi, M.; Jia, Y.; Zhang, P.; Cullen, D. A.; Xi, Z.; Lin, H.; Yin, Z.; Shen, B.; Muzzio, M.; Yu, C.; Kim, Y. S.; Peterson, A. A.; More, K. L.; Zhu, H.; Sun, S. Hard-Magnet L1<sub>0</sub>-CoPt Nanoparticles Advance Fuel Cell Catalysis. *Joule* **2019**, *3*, 124-135.
- (2) Yoo, T. Y.; Yoo, J. M.; Sinha, A. K.; Bootharaju, M. S.; Jung, E.; Lee, H. S.; Lee, B. H.; Kim, J.; Antink, W. H.; Kim, Y. M.; Lee, J.; Lee, E.; Lee, D. W.; Cho, S. P.; Yoo, S. J.; Sung, Y. E.; Hyeon, T. Direct Synthesis of Intermetallic Platinum-Alloy Nanoparticles Highly Loaded on Carbon Supports for Efficient Electrocatalysis. *J. Am. Chem. Soc.* **2020**, *142*, 14190-14200.
- (3) Wang, D.; Xin, H. L.; Hovden, R.; Wang, H.; Yu, Y.; Muller, D. A.; DiSalvo, F. J.; Abruna, H. D. Structurally Ordered Intermetallic Platinum-Cobalt Core-Shell Nanoparticles with Enhanced Activity and Stability as Oxygen Reduction Electrocatalysts. *Nat. Mater.* **2013**, *12*, 81-87.
- (4) Yu, S.; Yang, H. Design Principles for the Synthesis of Platinum–Cobalt Intermetallic Nanoparticles for Electrocatalytic Applications. *Chem. Commun.* **2023**, *59*, 4852-4871.
- (5) Zhang, L.; Zhang, J.; Tan, W.; Zhong, C.; Tu, Y.; Song, H.; Du, L.; Liao, S.; Cui, Z. Amorphous TiO<sub>x</sub> Stabilized Intermetallic Pt<sub>3</sub>Ti Nanocatalyst for Methanol Oxidation Reaction. *Nano Lett.* **2023**, *23*, 5187-5193.
- (6) Han, A.; Zhang, J.; Sun, W.; Chen, W.; Zhang, S.; Han, Y.; Feng, Q.; Zheng, L.; Gu, L.; Chen, C.; Peng, Q.; Wang, D.; Li, Y. Isolating Contiguous Pt Atoms and Forming Pt-Zn Intermetallic Nanoparticles to Regulate Selectivity in 4-Nitrophenylacetylene Hydrogenation. *Nat. Commun.* **2019**, *10*, 3787-3793.
- (7) Chen, X.; Kong, C.; Huang, H.; Chen, D.-L.; Wang, F.-F.; Zhang, F.; Zhu, W. Mechanism of Selective Hydrogenation of 4-Nitrophenylacetylene Using Pt–Zn Intermetallic Nanoparticles: The Role of Hydrogen Coverage. *J. Phys. Chem. C* **2021**, *125*, 23803-23812.
- (8) Wang, L.; Holewinski, A.; Wang, C. Prospects of Platinum-Based Nanostructures for the Electrocatalytic Reduction of Oxygen. *ACS Catal.* **2018**, *8*, 9388-9398.
- (9) Wu, J.; Yang, H. Platinum-Based Oxygen Reduction Electrocatalysts. *Acc. Chem. Res.* **2013**, *46*, 1848-1857.
- (10) Jung, W. S.; Lee, W. H.; Oh, H.-S.; Popov, B. N. Highly Stable and Ordered Intermetallic PtCo Alloy Catalyst Supported on Graphitized Carbon Containing Co@CN for Oxygen Reduction Reaction. *J. Mater. Chem. A* **2020**, *8*, 19833-19842.
- (11) Li, J.; Sun, S. Intermetallic Nanoparticles: Synthetic Control and Their Enhanced Electrocatalysis. *Acc. Chem. Res.* **2019**, *52*, 2015-2025.

- (12) Kulkarni, A.; Siahrostami, S.; Patel, A.; Norskov, J. K. Understanding Catalytic Activity Trends in the Oxygen Reduction Reaction. *Chem. Rev.* **2018**, *118*, 2302-2312.
- (13) Pan, X.; Yu, S.; Zhang, J.; Zhang, L.; Wang, L.; Song, H.; Du, L.; Liao, S.; Cui, Z. Universal Solid-Phase Seed-Mediated Synthesis of Monodisperse and Ultrasmall L1<sub>0</sub>-PtM Intermetallic Nanocrystals. *Chem. Mater.* **2023**, *35*, 2559-2568.
- (14) Cheng, H.; Cao, Z.; Chen, Z.; Zhao, M.; Xie, M.; Lyu, Z.; Zhu, Z.; Chi, M.; Xia, Y. Catalytic System Based on Sub-2 nm Pt Particles and Its Extraordinary Activity and Durability for Oxygen Reduction. *Nano Lett.* **2019**, *19*, 4997-5002.
- (15) Sandbeck, D. J. S.; Secher, N. M.; Speck, F. D.; Sørensen, J. E.; Kibsgaard, J.; Chorkendorff, I.; Cherevko, S. Particle Size Effect on Platinum Dissolution: Considerations for Accelerated Stability Testing of Fuel Cell Catalysts. *ACS Catal.* **2020**, *10*, 6281-6290.
- (16) Zhu, Y.; Peng, J.; Zhu, X.; Bu, L.; Shao, Q.; Pao, C.-W.; Hu, Z.; Li, Y.; Wu, J.; Huang, X. A Large-Scalable, Surfactant-Free, and Ultrastable Ru-Doped Pt<sub>3</sub>Co Oxygen Reduction Catalyst. *Nano Lett.* **2021**, *21*, 6625-6632.
- (17) Li, J.; Kou, J.; Xiang, Y.; Chen, M.; Zhang, J.; Zhan, X.; Zhang, H.; Wang, F.; Dong, Z. ZIF-8 Derived N-doped Porous Carbon Confined Ultrafine PdNi Bimetallic Nanoparticles for Semi-Hydrogenation of Alkynes. *Mol. Catal.* **2023**, *535*, 112865.
- (18) Bai, L.; Wang, X.; Chen, Q.; Ye, Y.; Zheng, H.; Guo, J.; Yin, Y.; Gao, C. Explaining the Size Dependence in Platinum Nanoparticle Catalyzed Hydrogenation Reactions. *Angew. Chem. Int. Ed.* **2016**, *55*, 15656-15661.
- (19) Rosen, D. J.; Foucher, A. C.; Lee, J. D.; Yang, S.; Marino, E.; Stach, E. A.; Murray, C. B. Microwave Heating of Nanocrystals for Rapid, Low-Aggregation Intermetallic Phase Transformations. *ACS Mater. Lett.* **2022**, *4*, 823-830.
- (20) Ma, Y.; Kuhn, A. N.; Gao, W.; Al-Zoubi, T.; Du, H.; Pan, X.; Yang, H. Strong Electrostatic Adsorption Approach to the Synthesis of Sub-Three Nanometer Intermetallic Platinum—Cobalt Oxygen Reduction Catalysts. *Nano Energy* **2021**, *79*, 105465.
- (21) Hu, S.; Li, W.-X. Sabatier Principle of Metal-Support Interaction for Design of Ultrastable Metal Nanocatalysts. *Science* **2021**, *374*, 1360-1365.
- (22) Dai, Z. R.; Sun, S.; Wang, Z. L. Phase Transformation, Coalescence, and Twinning of Monodisperse FePt Nanocrystals. *Nano Lett.* **2001**, *1*, 443-447.
- (23) Zhang, B.; Fu, G.; Li, Y.; Liang, L.; Grundish, N. S.; Tang, Y.; Goodenough, J. B.; Cui, Z. General Strategy for Synthesis of Ordered Pt<sub>3</sub>M Intermetallics with Ultrasmall Particle Size. *Angew. Chem. Int. Ed.* **2020**, *59*, 7857-7863.
- (24) Wang, T.; Liang, J.; Zhao, Z.; Li, S.; Lu, G.; Xia, Z.; Wang, C.; Luo, J.; Han, J.; Ma, C.; Huang, Y.; Li, Q. Sub-6 nm Fully Ordered L1<sub>0</sub>-Pt-Ni-Co Nanoparticles Enhance

- Oxygen Reduction via Co Doping Induced Ferromagnetism Enhancement and Optimized Surface Strain. *Adv. Energy Mater.* **2019**, *9*, 1803771-1803779.
- (25) Zhou, H. C.; Long, J. R.; Yaghi, O. M. Introduction to Metal-Organic Frameworks. *Chem. Rev.* **2012**, *112*, 673-674.
- (26) Qi, Z.; Pei, Y.; Goh, T. W.; Wang, Z.; Li, X.; Lowe, M.; Maligal-Ganesh, R. V.; Huang, W. Conversion of Confined Metal@ZIF-8 Structures to Intermetallic Nanoparticles Supported on Nitrogen-Doped Carbon for Electrocatalysis. *Nano Res.* **2018**, *11*, 3469-3479.
- (27) Lu, X.; Liu, Y.; He, Y.; Kuhn, A. N.; Shih, P. C.; Sun, C. J.; Wen, X.; Shi, C.; Yang, H. Cobalt-Based Nonprecious Metal Catalysts Derived from Metal-Organic Frameworks for High-Rate Hydrogenation of Carbon Dioxide. *ACS Appl. Mater. Interfaces* **2019**, *11*, 27717-27726.
- (28) Sun, T.; Xu, L.; Wang, D.; Li, Y. Metal Organic Frameworks Derived Single Atom Catalysts for Electrocatalytic Energy Conversion. *Nano Res.* **2019**, *12*, 2067-2080.
- (29) Al-Zoubi, T.; Zhou, Y.; Yin, X.; Janicek, B.; Sun, C.; Schulz, C. E.; Zhang, X.; Gewirth, A. A.; Huang, P.; Zelenay, P.; Yang, H. Preparation of Nonprecious Metal Electrocatalysts for the Reduction of Oxygen Using a Low-Temperature Sacrificial Metal. *J. Am. Chem. Soc.* **2020**, *142*, 5477-5481.
- (30) Chaemchuen, S.; Zhou, K.; Kabir, N. A.; Chen, Y.; Ke, X.; Van Tendeloo, G.; Verpoort, F. Tuning Metal Sites of DABCO MOF for Gas Purification at Ambient Conditions. *Microporous Mesoporous Mater.* **2015**, *201*, 277-285.
- (31) Ashberry, H. M.; Gamler, J. T. L.; Unocic, R. R.; Skrabalak, S. E. Disorder-to-Order Transition Mediated by Size Refocusing: A Route toward Monodisperse Intermetallic Nanoparticles. *Nano Lett.* **2019**, *19*, 6418-6423.
- (32) Read, C. G.; Biacchi, A. J.; Schaak, R. E. Au-Ge and Ag-Ge Heterodimers with Tunable Domain Sizes: A Supersaturation-Precipitation Route to Colloidal Hybrid Nanoparticles. *Chem. Mater.* **2013**, *25*, 4304-4311.
- (33) Qi, Z.; Xiao, C.; Liu, C.; Goh, T. W.; Zhou, L.; Maligal-Ganesh, R.; Pei, Y.; Li, X.; Curtiss, L. A.; Huang, W. Sub-4 nm PtZn Intermetallic Nanoparticles for Enhanced Mass and Specific Activities in Catalytic Electrooxidation Reaction. *J. Am. Chem. Soc.* **2017**, *139*, 4762-4768.
- (34) Han, X.; Wang, Q.; Zheng, Z.; Nan, Z.; Zhang, X.; Song, Z.; Ma, M.; Zheng, J.; Kuang, Q.; Zheng, L. Size-Controlled Intermetallic PtZn Nanoparticles on N-Doped Carbon Support for Enhanced Electrocatalytic Oxygen Reduction. *ACS Sustainable Chem. Eng.* **2021,** *9*, 3821-3827.

- (35) Han, S. W.; Park, H.; Han, J.; Kim, J.-C.; Lee, J.; Jo, C.; Ryoo, R. PtZn Intermetallic Compound Nanoparticles in Mesoporous Zeolite Exhibiting High Catalyst Durability for Propane Dehydrogenation. *ACS Catal.* **2021**, *11*, 9233-9241.
- (36) Weidenkaff, A.; Steinfeld, A.; Wokaun, A.; Auer, P. O.; Eichler, B.; Reller, A. Direct Solar Thermal Dissociation of Zinc Oxide: Condensation and Crystallisation of Zinc in the Presence of Oxygen. *Sol. Energy* **1999**, *65*, 59-69.
- (37) Anthrop, D. F.; Searcy, A. W. Sublimation and Thermodynamic Properties of Zinc Oxide. *J. Phys. Chem.* **1964**, *68*, 2335-2342.
- (38) Iihama, S.; Furukawa, S.; Komatsu, T. Efficient Catalytic System for Chemoselective Hydrogenation of Halonitrobenzene to Haloaniline Using PtZn Intermetallic Compound. *ACS Catal.* **2016**, *6*, 742-746.
- (39) Liu, Z.; Zhou, X.; Buchanan, D.; Kiss, J.; White, J. M. The Surface Chemistry of Vinyl Iodide on Platinum (111). *J. Am. Chem. Soc.* **1992**, *114*, 2031-2039.
- (40) Chen, G.; Xu, C.; Huang, X.; Ye, J.; Gu, L.; Li, G.; Tang, Z.; Wu, B.; Yang, H.; Zhao, Z.; Zhou, Z.; Fu, G.; Zheng, N. Interfacial Electronic Effects Control the Reaction Selectivity of Platinum Catalysts. *Nat. Mater.* **2016**, *15*, 564-569.
- (41) Wang, H.; Bai, S.; Pi, Y.; Shao, Q.; Tan, Y.; Huang, X. A Strongly Coupled Ultrasmall Pt<sub>3</sub>Co Nanoparticle-Ultrathin Co(OH)<sub>2</sub> Nanosheet Architecture Enhances Selective Hydrogenation of  $\alpha$ , $\beta$ -Unsaturated Aldehydes. *ACS Catal.* **2019**, *9*, 154-159.
- (42) Zheng, Q.; Wang, D.; Yuan, F.; Han, Q.; Dong, Y.; Liu, Y.; Niu, X.; Zhu, Y. An Effective Co-promoted Platinum of Co–Pt/SBA-15 Catalyst for Selective Hydrogenation of Cinnamaldehyde to Cinnamyl Alcohol. *Catal. Lett.* **2016**, *146*, 1535-1543.
- (43) Zheng, R.; Porosoff, M. D.; Weiner, J. L.; Lu, S.; Zhu, Y.; Chen, J. G. Controlling Hydrogenation of CO and CC Bonds in Cinnamaldehyde Using Silica Supported Co-Pt and Cu-Pt Bimetallic Catalysts. *Appl. Catal.*, A **2012**, 419-420, 126-132.
- (44) Merlo, A. B.; Machado, B. F.; Vetere, V.; Faria, J. L.; Casella, M. L. PtSn/SiO<sub>2</sub> Catalysts Prepared by Surface Controlled Reactions for the Selective Hydrogenation of Cinnamaldehyde. *Appl. Catal.*, A **2010**, 383, 43-49.
- (45) Goh, T. W.; Tsung, C.-K.; Huang, W. Spectroscopy Identification of the Bimetallic Surface of Metal–Organic Framework-Confined Pt–Sn Nanoclusters with Enhanced Chemoselectivity in Furfural Hydrogenation. *ACS Appl. Mater. Interfaces* **2019**, *11*, 23254-23260.
- (46) Chen, M.; Yan, Y.; Gebre, M.; Ordonez, C.; Liu, F.; Qi, L.; Lamkins, A.; Jing, D.; Dolge, K.; Zhang, B.; Heintz, P.; Shoemaker, D. P.; Wang, B.; Huang, W. Thermal Unequilibrium of PdSn Intermetallic Nanocatalysts: From In Situ Tailored Synthesis to Unexpected Hydrogenation Selectivity. *Angew. Chem., Int. Ed.* **2021**, *60*, 18309-18317.

- (47) Zhang, L.; Zhou, M.; Wang, A.; Zhang, T. Selective Hydrogenation over Supported Metal Catalysts: From Nanoparticles to Single Atoms. *Chem. Rev.* **2020**, *120*, 683-733.
- (48) Maligal-Ganesh, R. V.; Xiao, C.; Goh, T. W.; Wang, L.-L.; Gustafson, J.; Pei, Y.; Qi, Z.; Johnson, D. D.; Zhang, S.; Tao, F.; Huang, W. A Ship-in-a-Bottle Strategy To Synthesize Encapsulated Intermetallic Nanoparticle Catalysts: Exemplified for Furfural Hydrogenation. *ACS Catal.* **2016**, *6*, 1754-1763.

# TOC graphic

